

Article

The Liquid Jet Endstation for Hard X-ray Scattering and Spectroscopy at the Linac Coherent Light Source

Cali Antolini ^{1,†}, Victor Sosa Alfaro ^{1,†}, Marco Reinhard ¹, Gourab Chatterjee ¹, Ryan Ribson ¹, Dimosthenis Sokaras ¹, Leland Gee ¹, Takahiro Sato ¹, Patrick L. Kramer ¹, Sumana Laxmi Raj ¹, Brandon Hayes ¹, Pamela Schleissner ¹, Angel T. Garcia-Esparza ¹, Jinkyu Lim ^{1,2}, Jeffrey T. Babicz Jr. ¹, Alec H. Follmer ³, Silke Nelson ¹, Matthieu Chollet ¹, Roberto Alonso-Mori ^{1,*}, Tim B. van Driel ^{1,*}

- ¹ SLAC National Accelerator Laboratory, 2575 Sand Hill Road, Menlo Park, CA 94025, USA; calianto@slac.stanford.edu (C.A.); sosavic8@slac.stanford.edu (V.S.A.); marcor@slac.stanford.edu (M.R.); gourab@slac.stanford.edu (G.C.); ribson@slac.stanford.edu (R.R.); dsokaras@slac.stanford.edu (D.S.); lbgee@slac.stanford.edu (L.G.); takahiro@slac.stanford.edu (T.S.); pkramer@slac.stanford.edu (P.K.); slraj@slac.stanford.edu (S.L.R.); bhayes@slac.stanford.edu (B.H.); pam@slac.stanford.edu (P.S.); garciaat@slac.stanford.edu (A.T.G-E); jbabicz@slac.stanford.edu (J.T.B.); snelson@slac.stanford.edu (S.N.); mchollet@slac.stanford.edu (M.C.);
- ² Department of Energy and Environmental Engineering, The Catholic University of Korea, Bucheon 14662, South Korea; jinkyu@catholic.ac.kr (J.L.);
- ³ Department of Chemistry, University of California-Irvine, Irvine, CA 92697, USA; afollmer@uci.edu (A.H.F.);
- * Correspondence: roberto@slac.stanford.edu (R.A-M.); timbvd@slac.stanford.edu (T.v.D);
- + These authors contributed equally to this work.

Abstract: The ability to study chemical dynamics on ultrafast timescales has greatly advanced with the introduction of X-ray free electron lasers (XFELs) providing short pulses of intense X-rays tailored to probe atomic structure and electronic configuration. Fully exploiting the full potential of XFELs requires specialized experimental endstations along with the development of techniques and methods to successfully carry out experiments. The liquid jet endstation (LJE) at the Linac Coherent Light Source (LCLS) has been developed to study photochemistry and biochemistry in solution systems using a combination of X-ray solution scattering (XSS), X-ray absorption spectroscopy (XAS), and X-ray emission spectroscopy (XES). The pump-probe setup utilizes an optical laser to excite the sample, which is subsequently probed by a hard X-ray pulse to resolve structural and electronic dynamics at their intrinsic femtosecond timescales. The LJE ensures reliable sample delivery to the X-ray interaction point via various liquid jets, enabling rapid replenishment of thin samples with millimolar concentrations and low sample volumes at the 120 Hz repetition rate of the LCLS beam. This paper provides a detailed description of the LJE design and of the techniques it enables, with an emphasis on the diagnostics required for real-time monitoring of the liquid jet and on the spatiotemporal overlap methods used to optimize the signal. Additionally, various scientific examples are discussed highlighting the versatility of the LJE.

Keywords: XFEL; X-ray diffraction; X-ray scattering; X-ray absorption Spectroscopy; XANES; EXAFS; X-ray Emission Spectroscopy; Photochemistry; Biochemistry; Time-resolved X-ray studies

1. Introduction

X-ray free-electron lasers (XFELs) produce intense and ultrashort X-ray pulses, enabling a time-resolution on the tens of femtosecond timescales. This has led to a need for novel instrumentation specifically tailored to the unique characteristics of the XFEL facilities, including sample delivery [1–3], detectors [4–6], and real-time diagnostics [7–9]. Particularly, due to the extreme intensity of each individual XFEL pulse, sample delivery methods had to be developed to replenish the sample between X-ray pulses. The liquid jet endstation (LJE), centered around a recirculating liquid jet, has become a standard

Citation: To be added by editorial staff during production.

Academic Editor: Firstname Lastname

Received: date

Revised: date

Accepted: date

Published: date



Copyright: © 2024 by the authors. Submitted for possible open access publication under the terms and conditions of the Creative Commons Attribution (CC BY) license (<https://creativecommons.org/licenses/by/4.0/>).

method for studies of solution-phase systems at the Linac Coherent Light Source (LCLS) [10].

The LJE is designed for multimodal pump-probe studies employing a combination of techniques including wide-angle X-ray solution scattering (XSS), X-ray emission spectroscopy (XES) and X-ray absorption spectroscopy (XAS). These techniques are coupled with an optical laser system to photoexcite the solution-phase samples. This approach enables methods that uniquely probe the structure, spin and charge of solution-phase systems on their intrinsic femtosecond timescale with atomic resolution and elemental specificity. Overall, this system allows robust sample delivery in a versatile yet compact configuration to address the needs of the community targeting the study of photochemistry and biochemistry in solution-phase systems. The setup has undergone several iterations and has been successfully deployed to support various experiments and techniques highlighted herein.

Optimized for hard X-ray energies (5-25 keV), the LJE has been integrated in the X-ray Pump-Probe (XPP [11]), Macromolecular Femtosecond Crystallography (MFX [12]) and X-ray Correlation Spectroscopy (XCS [13]) instruments located in the Near and Far Experimental Halls (NEH/FEH) of the LCLS. For simplicity, this paper will focus only on the XCS instrument, where the system is primarily deployed. The general beamline components of XCS are discussed elsewhere [13].

2. XCS Instrument Overview

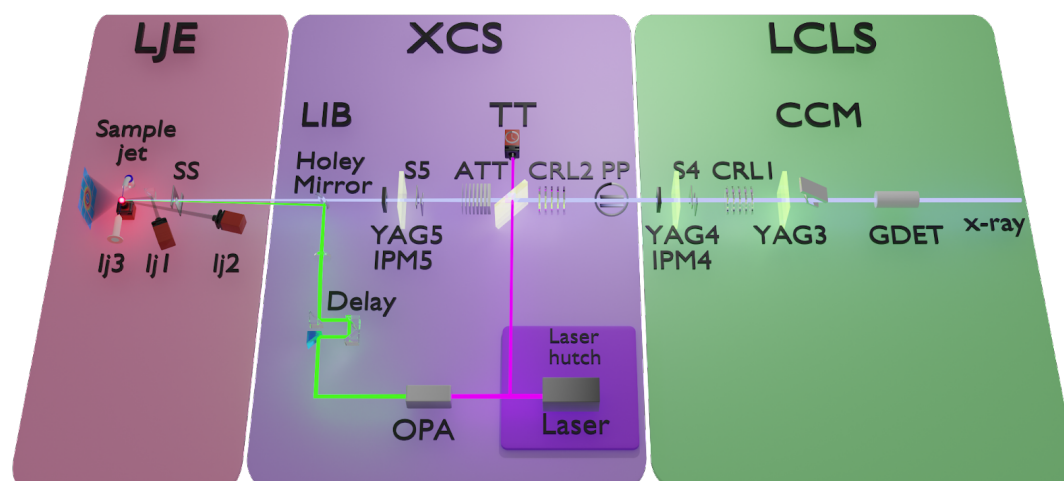


Figure 1. Essential LJE and XCS beamline components. Right) Upstream LCLS Components including a Gas Detector (GDET) for measuring the beam intensity, the scannable Channel-Cut Monochromator (CCM), YAG screens for beam position monitoring, X-ray Intensity Monitors (IPM4), slits (S4), and pre-focusing Compound Refractive X-ray Lenses (CRL1). Middle) XCS beamline components including a pulse picker/selector (PP), another set of focusing lenses (CRL2), attenuators (ATT), slits (S5), a YAG screen, an X-ray Intensity Monitor (IPM5) as well as the optical laser and time-tool (TT). The laser system is also depicted in the diagram. Left) the LJE setup including a recirculating liquid jet, sample viewing cameras (lj1-3) and clean-up sample slits (SS) as well as the XSS scattering detector (shown here) and/or a flavor of the XAS/XES setup (not shown here).

The XCS instrument, located in the FEH of the LCLS, operates in the hard X-ray regime from 5 keV to 25 keV. For measurements that don't require a monochromatic beam, the setup can use the full self-amplified spontaneous emission (SASE) beam (~ 30 fs, $\sim 3 \times 10^{-3} \Delta E/E$, 2×10^{11} ph/pulse at the sample) [11,13]. The system can also operate in a scannable monochromatic mode by inserting the channel-cut monochromator (CCM), (~ 30 fs, $\sim 1.4 \times 10^{-4} \Delta E/E$, $\sim 10^{10}$ ph/pulse at the sample) [14]. The SASE beam takes advantage of the first-harmonic properties of LCLS's main line and is also referred to as 'pink' beam.

86 The CCM uses Si(111) crystals to select a narrow X-ray bandwidth with an energy
87 resolution suitable for XAS core level spectroscopy, including X-ray absorption near edge
88 structure (XANES) [15] and extended X-ray absorption fine structure (EXAFS) [16] for
89 transition metal complexes. Other nonstandard operation modes can also be utilized (self-
90 seeding, multibunches, two-color, etc) [17,18].

91 As shown in **Figure 1**, general XCS instrument components include optics, slits and
92 diagnostics located upstream, these components help assist in beam alignment and
93 monitoring. Communal gas detectors (GDET) monitor the X-ray intensity providing real-
94 time information on X-ray stability. Two sets of compound refractive Beryllium lenses
95 (CRLs) are used to focus the beam size down to 3 to 100 μm at the sample location,
96 compared to the unfocused beam size of 1 mm \times 1 mm full width at half maximum
97 (FWHM). The typical spot size for the LJE experiments is around 20 μm (or approximately
98 half of the thickness of the liquid jet used). Horizontal and vertical slits are placed along
99 the beam path to aid in alignment and beam clean-up. The last set of slits are located inside
100 the LJE chamber to remove stray scattering at the X-ray/jet interaction point (IP), which is
101 approximately 100 mm downstream of the slits. Generally, placed after a set of slits are
102 yttrium aluminum garnet (YAG) scintillator screens that can be inserted in the beam path
103 to monitor the X-ray beam profile. Nondestructive intensity position monitors (IPMs),
104 composed of Si_3N_4 targets of different thickness (1, 2, 4 μm) and several diodes are used
105 to measure the photon count rates [7]. To prevent damage to detectors and important
106 optics, XCS is equipped with X-ray attenuators (ATT) and a pulse picker (PP). The ATTs
107 adjust the X-ray intensity on the downstream detectors and optics, while the PP can act as
108 a shutter to block the X-rays. The PP can also be used to reduce the X-ray repetition rate
109 [13].

110 When the XCS instrument uses the full SASE beam, it can operate concurrently with
111 the XPP instrument. In this operation mode a thin diamond crystal is inserted into the
112 beam path selecting a ~ 0.4 eV slice of the SASE energy bandwidth, which is used by XPP
113 [19], while letting the rest of the beam transmit downstream towards XCS. This allows for
114 XSS and XES experiments to be performed at the XCS instrument while compatible
115 experiments are performed at XPP. This concurrent operation mode is not compatible
116 with XCS operating in scannable monochromatic mode as for XAS type measurements.

117 2.1. XCS Pump Laser

118 The XCS ultrafast laser, used to optically excite the sample, is a Ti:sapphire laser
119 (Astrella, Coherent). The uncompressed output of 9.6 mJ at a repetition rate of 120 Hz
120 centered at 800 nm is delivered from an adjoining laser room and then compressed in the
121 XCS hutch to <40 fs with a double-pass grating compressor. A small fraction of the
122 compressed beam is sent to a spectral time-tool (TT) to measure the time delay between
123 the optical laser pulse and the XFEL [8,20]. The remaining compressed beam (6 mJ) can
124 then be frequency-converted via second (400 nm) or third (266 nm) harmonic generation,
125 or through optical parametric amplification (OPA). The OPA (Topas-Prime-HE and
126 NIRUVis, Light Conversion) can be spectrally tuned in the range 240-2600 nm, with a
127 maximum of ~ 1 mJ at signal wavelengths of 1300-1500 nm. For other wavelengths, the
128 output pulse energy depends strongly on the generation method (the non-linear
129 interactions between the pump, signal and idler in the OPA). Representative pulse
130 energies for some commonly used wavelengths are listed in **Table 1**. The laser focal spot
131 is typically 70 μm (FWHM) at the interaction point to maintain spatial overlap between
132 the laser and the XFEL, despite relative pointing jitter, whilst allowing for sufficient
133 fluence at the interaction point. Thin nonlinear crystals are used for frequency conversion
134 to maintain short pulse durations (<50 fs) at the cost of conversion efficiency since
135 microjoule-level energies are adequate for most liquid-phase chemistry experiments.
136 Occasionally, depending on experimental requirements and feasibility, post-compression
137 techniques (for instance, prism compression for 266 nm) may also be employed.

Table 1. Optical laser parameters.

Wavelength (nm)	Maximum energy (mJ)	Typical energy at IP (mJ)	Generation method
800	6	>1	Fundamental
400	1.2	0.8	2nd harmonic
266	0.25	0.05	3rd harmonic
500	0.7	0.2	OPA
600	0.5	0.1	OPA

The optical pump beam propagates nearly collinearly with the X-ray probe beam with a ~2 degree crossing angle at the sample position. This is achieved by combining the X-ray and laser beams using a holey mirror in a laser in-coupling box (LIB). The final position and overlap of the laser is fine-tuned by adjusting the horizontal and vertical position of the focusing lens, located before the LIB ($f = 750$ mm). The LIB is also equipped with a fast timing diode (with ~50 ps accuracy and ~200 ps time response) that records the X-ray and laser signals bouncing off a Ti target, monitored by a fast LeCroy oscilloscope [21,22].

The spectral time-tool allows for precise timing between the arrival of the laser and the XFEL at the interaction point. A broadband white-light continuum is generated from a few microjoules of the compressed laser pulse in a 1-2 mm thick sapphire crystal and temporally chirped. It is overlapped with the X-ray beam on a target – typically Ce-doped or Lu-doped YAG or Si₃N₄ [8,20,21]. The X-ray pulses release charge carriers in the target, transiently changing the optical transmission of the white light continuum through the target, which is monitored by a Czerny-Turner spectrograph. Thus, the linear chirp in the white light continuum spectrally encodes the arrival time of the X-rays, allowing to compensate for the inherent time-jitter in the X-rays due to the SASE process. The composition and thickness of the timing targets depend on the X-ray wavelength and intensity, since the transmission of X-ray pulses varies between materials [21,22]. Typically, a 2- μ m thick Si₃N₄ time-tool target is used for pink beam experiments. During monochromatic operation, given the reduced X-ray intensity, the time-tool target (20- μ m thick YAG) is often partially inserted into the X-ray path until a reliable TT signal is generated, which is known as ‘half-clipping’. The protocol for finding temporal overlap between the X-rays, the laser and the time-tool for precise shot-by-shot timing is described in detail at the end of next section.

3. Liquid Jet Endstation (LJE)

The liquid jet endstation comprises a complete sample delivery system equipped with diagnostics and detectors engineered for X-ray spectroscopy and scattering experiments on solution-phase samples. The rapidly flowing (1-15m/s) liquid jet ensures fresh sample after each probe pulse at the 120 Hz LCLS X-ray repetition rate [23,24]. This versatile sample delivery method allows for complex experiments for studying a wide range of solution-phase samples. Additionally, the LJE enables chemical reactions to be photo-triggered *in situ* and facilitates data analysis in shot-by-shot mode. In this section the liquid jet configuration is described in detail.

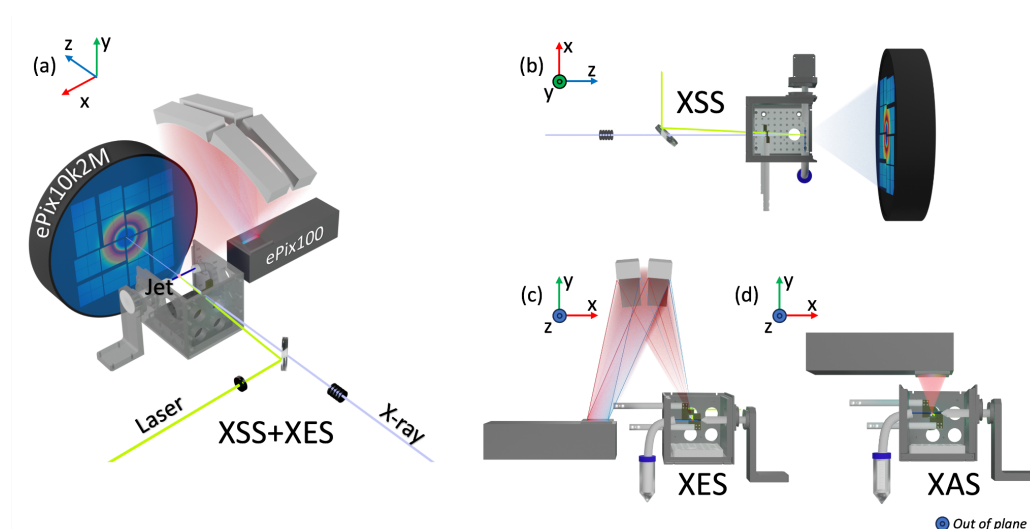


Figure 2. Schematics of the LJE for the 3 different techniques XSS, XES & XAS. (a) The XSS and XES setup seen from upstream. The X-ray beam (light purple) passes through the focusing lenses then the holey mirror before entering the sample chamber quasi-collinearly to the laser beam (lime). Both beams pass through clean-up slits (bronze) before the interaction point (red dot) with the sample from the liquid jet (blue). The liquid jet nozzle is placed in the positive x-direction, while the catcher tube and sample reservoir are placed in the negative x-direction of the chamber. The ePix10k2M detector is downstream from the interaction point. (b) The XSS setup seen from above. The ePix10k2M detector is located downstream from the interaction point. (c) The XES seen from downstream. A spectrometer is placed above the sample chamber focusing the emitted X-rays from the sample into the ePix100 detector. The detector is placed to the left (negative x-direction) of the sample chamber. (d) The XAS setup seen from downstream. The ePix100 detector is placed above the sample chamber to directly measure the total fluorescence yield. XSS can be measured simultaneously with either XES or XAS.

A He purged sample chamber, including sample monitoring and clean-up slits, houses the motorized liquid jet (see **Figure 2**). The sample chamber is made from aluminum with the downstream and top sides fitted with an L-shaped Kapton window to allow for X-ray detection while enclosing the sample. The window seals against the chamber with a thin foam gasket. The He environment is essential in decreasing the background produced by air scattering and air absorption as well as protecting oxygen sensitive samples from air exposure. In addition to purging the chamber, the sample reservoir is purged with He near the liquid surface to minimize the presence of oxygen. To minimize sample evaporation, the dry He purging the sample is bubbled through spare solvent. The design of the chamber was optimized to account for the vertical polarization of the LCLS incident X-ray beam by utilizing a horizontal jet. This allows for X-ray spectroscopies to be detected in the vertical direction where the elastic X-ray scattering due to the LCLS vertical X-ray polarization is minimal. The right side of the enclosure (positive x-direction in **Figure 2**) has an opening for the insertion of the liquid jet nozzle, while the left side (negative x-direction in **Figure 2**) contains a hole that is fitted with a catcher tube to facilitate recirculating or discarding of the sample. The positions of the jet nozzle and catcher tube are shown best in **Figure 2c** and **2d**. The liquid jet, driven by a Shimadzu high-pressure liquid chromatography (HPLC) pump (LC-20AD, LC-20AT, LC-20AP), delivers the sample into the interaction point. The pumps can be outfitted with polyether ether-ketone (PEEK) or polytetrafluoroethylene (PTFE) tubing permitting samples to be prepared with either aqueous or organic solvents. The HPLC pumps are also equipped with communication boards that allow for the pumps to be run in a remote-controlled mode. This mode is particularly useful to minimize sample usage and loss or sample exposure to oxygen. To observe sample degradation, an aliquot of sample can be used with a nearby NanoDrop UV-Visible spectrometer to observe changes in the

absorption spectrum. Alternatively, an in-line UV-Visible spectrometer can be used to monitor changes in the UV-Visible absorption spectrum related to sample degradation and solvent evaporation in real-time.

The LJE uses gasless cylindrical jets, or Rayleigh jets, with the option to vary the jet diameter through the choice of fused silica capillary nozzles with an inner diameter between 20 and 500 μm . The liquid jet thickness can be optimized for the sample concentration and optical absorption. Low concentration samples can benefit from thicker jets, however, trade-offs with time-resolution due to the velocity mismatch in the jet between optical pump and X-ray probe (further explained at the end of this section) [25–28] must be considered. Liquid jets with a diameter of 30, 50 and 100 μm are the most typically used based on these considerations. The LJE setup is compatible with the newly developed chip based liquid jet interface [3]. One available type of chips provides converging sheet jets with thicknesses ranging from 10 to 80 μm . The converging sheet jets require significantly higher flow rates and require a dampening volume to minimize pulsation, thereby increasing the sample volumes needed [2,3]. Converging sheet jets allow for thinner samples, where cylindrical jets require very high pressures to operate. Typical flow rates used to produce stable cylindrical jets are on the order of 0.5 to 3 ml/min depending on solvent and jet diameter whereas 30 to 50 ml/min is needed for sheet jets. Typically, the sample is recirculated from a reservoir consisting of a 50 ml Falcon tube to allow sufficient reservoir for the sample to settle and cover the inline filter for the HPLC pump. The dead volume is approximately 5 ml and a 20–45 ml sample volume is ideal for continuous operation. For samples prepared with volatile solvents where evaporation is a concern (solvent evaporation could amount up to 10 ml/hr), a syringe pump can be used to replenish the solvent remotely. For these cases, the LJE is equipped with a camera to monitor the volume of the sample reservoir. The converging sheet jet with increased flow speeds and including a dampening volume requires sample volumes in the 200–500 ml range. For irreversible reactions, either jet can be run without recirculation at the quoted 1–50 ml/min flow speeds resulting in 60–3000 ml/hr sample consumption.

Clear viewing, real-time monitoring and optimization of the liquid jet are critical for successful low noise data collection. The chamber walls of the He enclosure include viewing ports for multiple diagnostic cameras (15 Hz GigE and 120 Hz Alvium), depicted as lj1–3 in **Figure 1**. Various colored band pass filters are used according to the optical laser wavelength to protect the viewing cameras from damage due to excessive scattered laser light. Along with camera viewing, proper illumination of the jet is also needed, particularly when trying to observe the jet explosions initiated by the laser and/or X-ray beam. A continuous LED is used for ample viewing of the initial jet insertion, setup, and optimization, while a triggered and synchronized short pulse LED-array (1–50 μs) is used during experiments as viewing the jet explosions can be used to find and monitor the spatiotemporal overlap.

The LJE is equipped with two area detectors, the ePix10k2M and ePix100, used both for diagnostics and data collection. The ePix family of detectors was developed at SLAC prioritizing noise, dynamic range, and linearity across X-ray energies [4,6,29]. An overview of the ePix detectors is given in **Table 2**. The ePix10k2M has 3 gain modes: low, medium, and high gain providing different noise performance and dynamic range.; for further information regarding the detectors refer to Blaj *et al.* (2019) and van Driel *et al.* (2020).

Table 2. Detector parameters.

	ePix10k2M (L/M/H)	ePix100
Saturation (8 keV photons)	10000/300/100	100
Pixel size	100 μm x 100 μm	50 μm x 50 μm
Noise (8 keV photons RMS)	1.7/0.07/0.04 photons	0.026
Frame rate	120 Hz	120 Hz

As depicted in **Figure 2b**, the ePix10K2M is placed ~45-150 mm downstream of the sample chamber to optimize the detection of the XSS signal at high scattering angles in the forward scattering direction. A hole in the center of the ePix10k2M detector along with a hollow steel tube extending from the detector hole to the sample chamber Kapton window, allows for the transmitted X-ray beam to pass through without damaging the detector or adding a large air scattering background to the detected signal. Due to large variations in scattering signal strength across the detector area, mixed gain modes can be applied to the ePix10k2M detector [4,6]. The ePix100 is positioned either above (for XAS measurements) or to the side (for XES measurements) of the sample chamber (see **Figure 2c and 2d**). The position of the ePix100 detector is dependent on the technique used and is described in further detail in the next section.

Pump-probe experiments rely on the precise spatial overlap between the X-ray and laser beams at the sample position. This process is initiated with a visual alignment of the two beams utilizing a retractable frosted YAG screen at the interaction point. After the visual laser/X-ray spatial alignment, the liquid-jet is placed at the IP and the spatial overlap is optimized by scanning the laser position vertically and horizontally while monitoring both the jet explosions and resulting loss of the liquid scattering signal on the ePix10k2M at a time delay of 1 μ s. Jet explosions for most solvents occur when the pump laser energy is above the non-linear threshold (~1 TW/cm²) or the focused X-ray probe beam, in pink beam mode, is above ~0.2 mJ. This allows for an efficient and effective method to find spatial overlap of the liquid jet with the quasi-collinear X-ray and laser beams.

Temporal overlap (up to ~50 ps) between the X-rays and the laser pulse can be achieved using the signal from a Ti target, detected with a fast-timing diode and monitored on a LeCroy fast oscilloscope. The Ti target and diode can be inserted in the beam path remotely and the laser attenuated to yield an equivalent response on the fast diode. The laser delay is then adjusted to overlap with the X-ray reference trace on the oscilloscope. This is done both at the TT location and in the LIB, directly upstream of the LJE, which is a good proxy for the final timing at the sample position. At the TT, spatial overlap between the X-rays and the white light is achieved by inserting and monitoring a retractable frosted YAG screen while optimizing the white light position. After finding rough timing in the TT as described above, a binary search with the laser delay is performed while monitoring the X-ray induced change in refractive index of the time-tool target (typically Si₃N₄ or YAG), until fine time zero is found within ~50 fs and centered within the ~1 ps TT time window. One in, typically, 137 X-ray pulses is aborted by means of an electromagnet in the undulator hall with the purpose of obtaining X-ray dark references for the TT. In order to retain the TT timing signal, a delay stage is used to correct for delays up to ~1 ns. A timing drift monitoring script is used to automatically adjust the electronic delay of the laser and correct for timing drifts [21]. Following fine timing on TT, delay scans between the laser and X-ray pulses are conducted to find time-zero at the interaction point, achieving full spatio-temporal overlap.

Pump-probe experiments are typically conducted by changing the relative arrival time of the laser with respect to the X-rays via a number of delay stages and electronic delays. The laser delay can be controlled by an electronic delay for delays ranging from picoseconds up to milliseconds. For delays less than ~1 ns, the TT can be utilized since a separate delay stage can compensate for the path/delay to the TT, while scanning the overall laser delay electronically. This TT delay stage is initially adjusted to account for different path lengths in the laser setup, and also compensates for a chosen delay between the IP and TT. Finally, fast time scans are achieved by continuously scanning an encoded delay stage (<330 ps total range). The stages are all set to 0 at nominal time zero, thus the delay for recorded data on short timescales is composed solely of the fast delay value from the encoded delay stage and the TT correction. In the case of longer delays where the TT is out of range the delay is given by the electronic delay and the encoded delay stage. The best approach for data collection results from using the fast encoded continuous delay

stage, which allows for sweeping the delay rapidly within a given delay range [21]. The continuous scanning allows for a 100% duty cycle and minimizes the effect of drifts as temporal statistics are spread out in the measured delay range. This minimizes systematic temporal errors, especially when calculating difference signals from nearby unpumped shots. In order to record such unpumped reference data needed for analysis, the pump laser pulse is periodically delayed by ~40 ns to arrive after the X-rays. These “laser off” shots are typically taken once in every seven X-ray pulses, although this frequency can be optimized to maximize the signal-to-noise of the analyzed data. The TT signal (~25 fs FWHM) allows for post sorting data within the 200-300 fs gaussian temporal jitter of the LCLS X-ray beam. Based on this timing jitter, a stepwise scan comprised of <200 fs steps can be rebinned based on the TT values to generate a continuous delay map with a time resolution given by the instrument response function (IRF).

The IRF full width at half maximum (FWHM) of the system can be determined by analyzing the rise of a prompt sample signal. It can also be estimated *a priori* if X-ray pulse duration (P_{Xray}), laser pulse duration (P_{Laser}), time-tool response (TT), and jet thickness (d_{jet}) response is known, using the following equation:

$$IRF\ FWHM = \sqrt{(P_{Xray}\ fs)^2 + (P_{Laser}\ fs)^2 + (TT\ fs)^2 + (d_{jet} \times GVM\ fs/\mu m)^2}, \quad (1)$$

where the group velocity mismatch (GVM) for the laser and X-ray pulses is typically on the order of 1 fs/ μ m, depending on solvent and laser wavelength [25,26,28]. The typical LJE IRF is <90 fs FWHM for a 50 μ m sample jet and the best achieved time resolution without compressing x-rays and laser further was 65 fs FWHM for a 30 μ m sample jet.

Power titration measurements are generally conducted to evaluate the optimal pump laser power to linearly excite the sample. When the magnitude of the difference scattering signal increases linearly with laser fluence, the sample remains in the linear photoexcitation regime, not subject to multiphoton effects [30]. The nonlinear solvent multiphoton excitation recorded via XSS can be used to calibrate the laser power density or generate large signals for spatial alignment as explained above. The optimal laser power for experiments is typically a compromise between signal-to-noise and minimal to no multiphoton excitation. For experiments relying on polarization selectivity, the excitation fraction should further be kept below 30%.

4. Techniques

Since many biochemical and photochemical complexes contain transition metals [26,31–34], hard X-ray scattering and spectroscopic methods are valuable techniques to study the dynamics and structure of such complexes. A brief description of the commonly used techniques in the LJE and their respective experimental setups are given in this section.

4.1. X-ray Solution Scattering (XSS)

Time-resolved spectroscopic techniques such as optical transient absorption (OTA) as well as vibrational spectroscopies such as resonant impulsive stimulated Raman scattering (RISRS) and coherent anti-Stokes Raman scattering (CARS) cannot provide direct access to bond lengths and angles. Instead, researchers must rely on indirect probes and simulations to explore the dynamic structure and potential energy landscape of molecules. XFEL sources offer structurally sensitive probes with sub-picosecond time resolution, enabling direct measurement of bond-length and bond-angle dynamics following photoexcitation. XSS is used to directly probe the molecular structure and dynamics of disordered samples [27,34,35], and it is an integral technique used at the LJE in both experimental and diagnostic capacities.

The ePix10k2M detector, running at 120 Hz, collects an image of the scattering signal for each X-ray pulse with a given laser delay. The XSS signal is linearly correlated with

364 incident X-ray beam intensity measured by the beamline IPMs, and fluctuations in the
365 correlation slope are a convenient way to monitor, in real-time, X-ray beam or jet drifts.
366 The recorded scattering images are then azimuthally integrated and converted to the
367 difference scattering signals $\Delta S(q,t)$. At 9.5 keV, Q-ranges of $0.35\text{--}5.5\text{\AA}^{-1}$ and $0.1\text{--}3\text{\AA}^{-1}$ can
368 be achieved since the ePix10k2M detector is generally placed 40–150 mm downstream of
369 the interaction point.

370 The acquired difference scattering signal, ($\Delta S = S_{\text{laser on}} - S_{\text{laser off}}$), contains the scattering
371 difference from all atoms in the probed volume but is typically separated into three
372 distinct time resolved components consisting of changes in the solute, solvation cage and
373 the bulk solvent as follows [27,34,35]:

$$\Delta S(q,t) = \Delta S_{\text{solute}}(q,t) + \Delta S_{\text{solvation cage}}(q,t) + \Delta S_{\text{bulk solvent}}(q,t). \quad (1)$$

374 The solute component (ΔS_{solute}) describes the signal from the solute structural change
375 alone. It captures the intramolecular dynamics and is typically modeled using the
376 independent atom model based on predicted/simulated structures. The solute-solvent
377 component, also known as the solvation cage ($\Delta S_{\text{solvation cage}}$), highlights changes related to
378 solvation dynamics. The information provided through analysis of this component is site
379 specific and is a molecular perspective unrelated to the continuum descriptions of the
380 solvent. This signal is typically simulated using quantum mechanics/molecular mechanics
381 (QM/MM) or molecular dynamics (MD) approaches [36,37] or quantitatively analyzed.
382 The last component observes changes in bulk solvent ($\Delta S_{\text{bulk solvent}}$) structure [35], typically
383 well described by a temperature and density response. These responses can be measured
384 separately using a dye to efficiently deposit heat [38] into the solvent. By separating the
385 signal into these three separate terms the analysis can often be simplified and based on a
386 structural model, solvent reference measurements and MD simulations.

387 4.2. X-ray Absorption Spectroscopy (XAS)

388 XAS is a powerful technique for investigating the local geometric and electronic
389 structure with element specificity in complex systems [39,40]. When X-ray photons with
390 an energy above the binding energy of a core shell excite a sample, an absorption edge
391 arises corresponding to the transition between the core electrons and the unoccupied
392 valence states. This is characteristic of each individual element allowing XAS to be utilized
393 as an element-specific technique.

394 XAS can be separated in two distinct regions, resulting in two complementary
395 techniques, XANES and EXAFS. The XANES region, composed of the pre-edge and edge
396 structures arising from the probed unoccupied states, contains information on
397 oxidation/spin state and local geometry, i.e. symmetry and coordination. The EXAFS
398 region provides local structural information regarding the atom's environment, including
399 details on the coordination number, distance of neighboring atoms, and disorder of
400 neighboring atoms. Most experiments using the LJE focus on the XANES region. EXAFS
401 is less common, in part due to the technical challenges associated with it, but its feasibility
402 for dilute samples has been demonstrated by Britz *et al.* (2020). After absorption of an X-
403 ray and the concomitant excitation of a core electron, higher-lying electrons can fill the
404 core hole and, in the process, emit X-ray photons. By collecting this X-ray fluorescence as
405 a function of incident X-ray energy, the XAS spectrum can be constructed from the total
406 fluorescence yield (TFY). In standard XAS LJE experiments, the TFY signal is detected by
407 an ePix100 detector located vertically above the IP along the vertical polarization of the
408 LCLS beam in order to minimize the unwanted elastic scattering background (see **Figure**
409 **2d**). With this experimental setup, we are able to routinely measure 3d transition metal K-
410 edge and 5d transition metal L-edge XAS. The $>500\text{ eV}$ energy resolution of the ePix100
411 detector has a limited capability to differentiate XAS-related photons from the
412 background, and the stochastic nature of the XFEL beam together with jet instabilities
413 require a good normalization protocol. The XAS spectra are normalized to the solvent
414 scattering XSS collected by the ePix10k2M detector in the forward scattering direction,

415 which accounts for beam intensity variations as well as variations in the probed volume
416 of the liquid jet.

417 A typical pump-probe experiment using the LJE requires a sample concentration of
418 at least 1 mM of the transition metal of interest. Efforts to push the lower concentration
419 limit well below 1 mM based on the development of novel high throughput spectrometers
420 are underway and will be discussed elsewhere. To monitor the fidelity of the spectral data
421 and ensure scan accuracy, a metal foil of the element of interest and a diode are installed
422 downstream of the ePix10k2M. The diode collects the foil spectrum using the beam
423 transmitted after the liquid jet concomitantly with the spectrum from the actual sample.

4.3. X-ray Emission Spectroscopy (XES)

424
425 Hard X-ray XES on 3d transition metals relies on measuring K-line emission from
426 higher-level electrons filling the 1s vacancy, including the $K\alpha$, $K\beta$, and $K\beta_{2,5}$ or valence-to-
427 core (VtC) emission lines [26,34]. Time-resolved XES can be used to observe changes
428 associated with oxidation state and spin configurations ($K\alpha$ and $K\beta$), and metal-ligand
429 interactions such as hybridization due to bonding geometry and the nephelauxetic effects
430 due to bond lengths ($K\beta$ and VtC).

431 For XES experiments, the LJE can be equipped with a suite of multi-crystal
432 spectrometers of different geometries. The most common is an energy dispersive 4-crystal
433 analyzer spectrometer based on the 16 crystal analyzer von Hamos spectrometer
434 previously described by Alonso-Mori *et al.* in 2012 that enables the collection of full spectra
435 in a shot-by-shot basis [41]. A 3-crystal Rowland spectrometer, hosting spherical focusing
436 crystal analyzers, is also available for scanning applications. Resonant and non-resonant
437 photon-in photon-out techniques (XES, HERFD, RIXS...) are thus compatible with the LJE.
438 The spectrometer is placed above the sample interaction point in the He chamber to
439 minimize the unwanted scattering due to the vertical polarization of the LCLS X-ray
440 beam. A 3d-printed He-filled cone is placed in between the spectrometer and the chamber
441 to reduce the air attenuation of the signal, as shown in **Figure 2c**. The final positions of the
442 detector and the von Hamos or Rowland spectrometers are determined by the Bragg angle
443 of the emission lines being detected (these angles and geometries may be calculated using
444 web-based tools [42]). Each crystal analyzer has its own 3-point motorization for easy
445 alignment. The composition of the crystal analyzers used is dependent on the emission
446 lines desired to be measured and can cover the VtC, $K\beta_{1,3}$, and $K\alpha$ emission lines of most
447 3d transition metals. Multiple XES lines can be measured simultaneously if they have
448 comparable Bragg angles. The ePix100 has a sensor dimension of 40 mm along the energy
449 dispersion axis which corresponds to roughly 4.3 degrees of range of Bragg angle at values
450 >70 degrees with 250 mm radius of curvature crystals. For example, a popular user
451 configuration is to utilize $\text{LiNb}_2\text{O}_3(234)$ and $\text{Ge}(620)$ for Fe $K\alpha$, $K\beta$, and VtC XES
452 simultaneously. At 6404 eV (Fe $K\alpha_1$) and 7120 eV (VtC) the two signals encompass the two
453 ends of the energy dispersion axis of the detector with a difference in Bragg angle of 4.0
454 degrees. However, the Fe $K\alpha_2$ signal has a difference in Bragg angle of 4.7 compared to
455 the VtC and collection of the two features are mutually exclusive with a single detector.

4.4. Simultaneous Data Collection

456
457 Time-resolved XSS and X-ray spectroscopic measurements allow observation of
458 changes to the metal-ligand bonds (XSS) [26,35,37], charge and spin state of the metal
459 center (XES) [26,43], and oxidation state and local geometry/symmetry of the metal center
460 to be observed (XAS) [25,44,45]. The LJE is designed to allow simultaneous XSS and hard
461 X-ray spectroscopic measurements, which permits complementary information to be
462 collected within a single scan. Data collection and data analysis of XSS pairs well with the
463 methods used for XES measurements [46,47]. XSS and XES measurements take a similar
464 amount of time to complete and are optimal for pink beam operation. The full
465 unattenuated pink beam can be used to conduct the simultaneous XSS/XES experiments

466 since the ePix10k2M can extend the dynamic range. For a typical 20 mM Fe containing
467 sample in water and with 2 mJ XFEL pulses, the measured signal is far from saturation in
468 low gain at 30% of the dynamic range.

469 However, pairing XSS and XAS measurements is less ideal because XAS
470 measurements are performed using the less intense monochromatic X-ray beam and the
471 X-ray energy is constantly being scanned, which affects the resulting XSS scattering
472 pattern. Nevertheless, for XAS measurements the XSS data is still collected and used for
473 normalization. This is described in more detail by Britz et al. (2020). The XSS recorded
474 during a monochromatic XAS scan results in the collection of anomalous solution
475 scattering and holds additional structural information through the change in the
476 scattering form factor across the metal edge. However, further development of analysis
477 and experimental protocols is still needed for utilization of this A-XSS signal during XFEL
478 beamtimes.

479 4.5. Data Processing

480 Full detector images and associated parameters acquired at the LCLS are recorded
481 at 120 Hz and stored as large .xtc files. The data can then be processed in the Photon
482 Science Analysis (PSANA) python framework. PSANA has further been used to develop
483 the so called “smalldata” framework, which conveniently extracts and reduces the
484 necessary parameters and writes them to a smaller .hdf file where information pertaining
485 to each individual pulse is collated. A typical 6 minute delay scan with the ePix10k2M
486 produces 225 Gb of raw data and 260 Gb when including the ePix100 for spectroscopy.
487 Depending on the binning and ROI this typically reduces to a 1.1 Gb smalldata file for XSS
488 or 10-30 Gb for spectroscopy as saving a large ROI takes up more space. Thus the
489 smalldata framework reduces the data between a factor of 10-200. A primary method of
490 reduction of data into smalldata is the reduction of the detector images; either by selection
491 of regions of interest, commonly used for XAS and XES measurements, or by the binning
492 of pixels into larger bins, used for XSS processing.

493 Based on smalldata, analysis can be rapidly performed in a programming language
494 of choice such as python, matlab or julia. Python is in general recommended and example
495 scripts are made available on request and as a part of beamtime preparation. Typical
496 analysis involves filtering the data based on the shot-to-shot information such as X-ray
497 intensity and time-tool signal quality. Additional filtering can be performed using the XSS
498 signal, such as filtering on the correlation between the XSS and upstream IPMs, and such
499 filters can be applied to simultaneously measured XAS or XES datasets to improve their
500 fidelity. The XSS signal can also be used for normalization of shot-to-shot fluctuations in
501 signal intensities, either using the entire scattering signal or a select q region. Following
502 normalization to minimize noise, an average of all laser off shots is generally completed
503 to construct the “laser off” reference used for calculating difference signals. To account for
504 drifts, a selection of laser off shots (typically 50 or 100 shots) adjacent in time to the “on
505 shot” of interest can be used instead. The time delay axis is generated by adding the
506 nominal optical laser/X-ray delay and the time-tool correction (TTcor). Shots are binned
507 relative to this time delay and ultimately, 2D maps of $\Delta S_{\text{XSS}}(\vec{q}, t)$, $\Delta I_{\text{XAS}}(E, t)$ or
508 $\Delta I_{\text{XES}}(\vec{e}, t)$ are generated for further comparison with references or modeling.

509 5. Data Collection Examples

510 As described above, the XCS liquid jet configuration accommodates different X-ray
511 techniques that encompass a variety of scientific investigations ranging from materials
512 science, chemistry, and biology. The following section showcases some capabilities
513 enabled by the LJE with specific examples discussed in greater detail.

514 5.1. X-ray Absorption Spectroscopy

XAS has found widespread application in various time-resolved studies to help understand atomic and electronic dynamics of photoexcited processes at LCLS. Mara *et al.* used time-resolved Fe XANES to investigate the fast kinetics of cytochrome C thioether-Fe bond. They followed the Fe(II)-S(Met) bond rupture and recombination of a five coordinated high spin active site and quantified a protein contribution of 4.0 kcal mole⁻¹ to keep the S(Met) bound under physiological conditions, allowing bond rupture at room temperature and opening a catalytic ligand binding site as peroxidase in apoptosis [48].

As an illustrative example, a 50 μm diameter cylindrical jet was used to flow a 30 mM aqueous potassium ferricyanide, $\text{K}_3\text{Fe}(\text{CN})_6$ solution through the X-ray path, where it was photoexcited with a 266 nm pump laser with a fluence of ~ 100 mJ/cm² (~ 1.5 photons/molecule). **Figure 3a** shows the steady-state XANES spectra for $\text{K}_3\text{Fe}(\text{CN})_6$ collected from an average of 33 runs (~ 6.5 min/run, total ~ 215 min collection time). The observed features from this solution spectra are comparable to previously reported spectra [49–51]. This low-spin ferricyanide complex with an octahedral iron site (see inset in **Figure 3a**) has weak electric quadrupole allowed $1s \rightarrow 3d$ pre-edge features at about 7111.3 eV and 7114.3 eV [52]. Additionally, **Figure 3a** highlights the early picosecond transient XAS spectrum. The transient spectrum shows a ~ 2 eV blue shift of the absorption edge after photoexcitation of the ferric $\text{Fe}(\text{CN})_6$. It has been shown previously that the features in the pre-edge region are indicative of electronic and geometric structure changes [44,45]. The transient kinetic trace at 7.126 keV, **Figure 3b**, for aqueous $\text{K}_3\text{Fe}(\text{CN})_6$ was fitted with an IRF of ~ 152 fs.

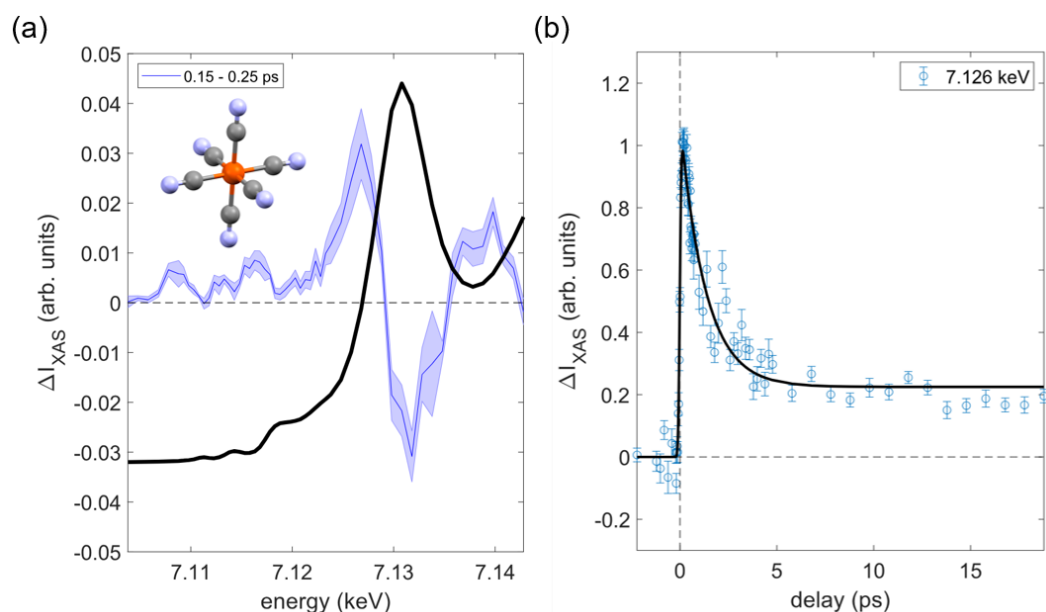


Figure 3. (a) XANES steady-state spectrum of aqueous ferricyanide, 30 mM, (shown in black) reveals a pre-edge assigned to the $1s\text{-}3d$ (t_{2g}) transition at 7.1113 keV and the $1s\text{-}3d$ (e_g) transition at 7.1143 keV. The transient X-ray absorption spectra of ferricyanide, recorded 0.15–0.25 ps after photoexcitation at 266 nm (shown in blue). (b) The kinetic trace for a single energy at 7.126 keV, along with the corresponding fit (shown in black). These transient absorptions were measured at the Fe K-edge using the liquid jet pump-probe method at XCS.

Another notable illustration of the applicability of XANES at XFELs comes from the use of picosecond time-resolved polarized XANES at the Co K-edge in a series of experiments at LCLS [53–55]. Sension *et al.* studied the long-lived photoexcited states of vitamin B₁₂ and derivatives, and observed spectral changes in both the equatorial and axial directions, indicative of a photoexcited structural changes within a time delay of 100 ps. In addition to XANES they also combined time-resolved XES to further probe

551 photoexcited dynamics [53,54]. Recently, Cammarata *et al.*, showcased the ability to
552 conduct simultaneous Co and Fe K-edges XANES time-resolved spectroscopy. Their
553 study gained further insight on the photoinduced charge transfer and ultrafast transition
554 dynamics between Co and Fe from their Prussian blue cyanide bridged CoFe complex
555 [56]. Specifically, they observed a spin transition occurring on the Co site within the first
556 ~50 fs which subsequently facilitated the transfer of charge from Fe to Co within ~200 fs.
557 XAS can also be synergistically combined with XSS to provide a reliable approach for
558 accurately assessing the interaction between electronic and structural components within
559 molecular complexes. For example, a recent study utilized XAS as a complementary
560 method for tracking solvent reorganization and recombination dynamics following the
561 photoabsorption of an electron from the aqueous I⁻ ion [57].

562 The electronic structure of 5d metals makes them unique for multiple applications in
563 catalysis, biology, cancer research, and photochemistry. Since 5d metals exhibit high
564 catalytic activity and tunability, they enable the design of selective catalysts for
565 challenging chemical transformations and energy conversion. With partially filled 5d
566 orbitals, metal complexes absorb light across a wide range of wavelengths which makes
567 them suitable for the utilization of a large portion of the solar spectrum in photocatalytic
568 and artificial photosynthesis applications. In biology, 5d metals can provide insights into
569 the biological roles of essential elements, and for the development of metalloenzymes with
570 novel functionalities. Furthermore, 5d metals can act as therapeutic agents or probes for
571 targeted light-driven drug delivery, such as complexes containing Pt and Ir used for
572 photodynamic therapy for cancer treatment [58–60].

573 **Figure 4** shows the Pt L₃-edge XANES of 1 mM hexachloroplatinate in an aqueous
574 pH neutral solution to demonstrate the feasibility and capability of studying 5d metals
575 using the LJE at LCLS (average of two scans, 10 minutes per scan). A 100 μm diameter jet
576 was used to flow the sample to the IP, where the sample was photoexcited at 266 nm with
577 a 150 μm spot diameter at 27 μJ resulting in a fluence of 153 mJ/cm² (ca. 34
578 photons/molecule). Laser power titrations showed a linear response at the selected laser
579 fluence. The Pt L₃-edge XANES absorption edge peak corresponds to the promotion of a
580 2p_{3/2} electron to the 5d orbital, often referred to as the “white-line” [61,62]. The white line
581 intensity decreases, and the absorption edge shows a blue shift upon UV-light excitation.
582 The overall intensity gives information on the occupation of the Pt 5d orbitals and thus
583 shape, position and intensity correlates to the oxidation state of the metal and its local
584 environment. Based on previous operando XAS electrochemical studies of Pt in aqueous
585 conditions [63], the observed changes in the white line at 10 ps after photoexcitation
586 qualitatively show the partial reduction of the Pt(IV) species in solution. Our results
587 appear consistent with an inner-sphere electron transfer resulting in the formation of a
588 radical with a few picoseconds lifetime and its subsequent photoaquation [64]. Transient
589 absorption spectroscopy was used to ascribe the fast formation (ca. 600 or 700 fs) of a
590 Pt^{III}Cl₅²⁻ or other unidentified intermediates to a short lived lifetime of 8.6 ps after 355 and
591 405 nm laser excitation [63,64]. First principles XAS calculations are underway and will be
592 reported elsewhere for the identification of the precise nature of the observed reduced
593 species. Understanding the dynamics and photophysics of these metals in chemistry and
594 biology will help us design new catalysts, materials, and medicines.

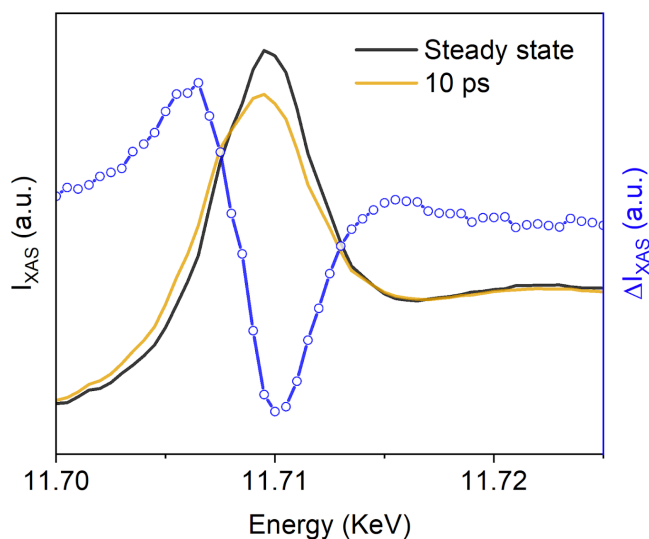


Figure 4. Pt L₃-edge XANES steady-state spectrum of aqueous hexachloroplatinate (1 mM K₂PtCl₆) (black line), the transient X-ray absorption spectrum after 10 ps photoexcitation at 266 nm (gold line) and the associated 10 ps difference spectrum (blue line).

Time-resolved XAS with the LJE has also been extensively used for investigating structural changes of biomolecules with femtosecond time resolution. Such is the case with the carbon monoxy-myoglobin (MbCO) complex [65–67]. Noteworthy, the Fe(II) K-edge XANES spectrum of Mb-CO photoproduct has been reported and shown to be sensitive to the structural changes within the heme iron. In particular, it is sensitive to the distance between the Fe and the N_ε of the proximal histidine [32,33]. This change occurs within ~400 fs after photolysis of MbCO [65], as shown by the Fe K-edge energy red-shifts to 7125 KeV, respectively, compared to the MbCO static spectrum [31]. **Figure 5** highlights a MbCO Fe K-edge time-resolved XAS photolysis measurement done with the LJE. A 532 nm wavelength pump laser, with 7 μJ focused to 250 μm at the sample position, was used for excitation into the heme Q bands. MbCO was generated by reducing the ferric Mb with dithionite at concentrations between 4–8 mM followed by bubbling excess CO through the solution and confirmed the conversion to Fe²⁺-CO bound species by UV-visible spectroscopy. The sample, a 4 mM aqueous solution of MbCO, was flown through a 50 μm capillary jet. The data was collected by simultaneous scanning of the CCM and of the fast delay stage, yielding 2D datasets binned over energy and time. The data in **Figure 5** show the averaged kinetics trace at 7125 eV from 14 runs, ~70 min data collection, reflecting the edge shift to lower energies after Mb-CO photolysis. This results in a signal that grows in with a time constant of 290 fs and does not decay in the time window observed. This is comparable to the 170 ps time constant that was observed by Levantino *et al.* in 2015. However, due to the fitted IRF of 160 fs, the 70 fs time constant, which was also observed by Levantino *et al.* (2015), was not found.

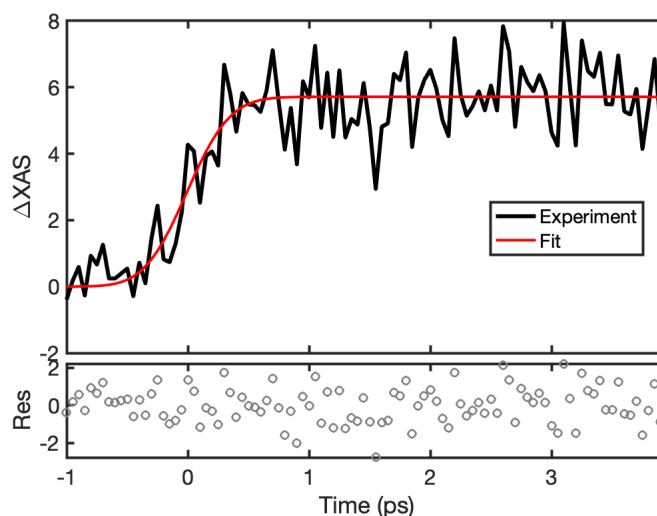


Figure 5. XANES intensity at the Fe K-edge (7125 eV) after 532 nm photolysis of MbCO. The time trace is binned at 50 fs intervals from -1 to 4 ps delay times, then fit to a single exponential function convolved with a gaussian instrument response function. The fit provides a mono-exponential rate constant of $\kappa = 3.45$ ($\tau = 290$ fs).

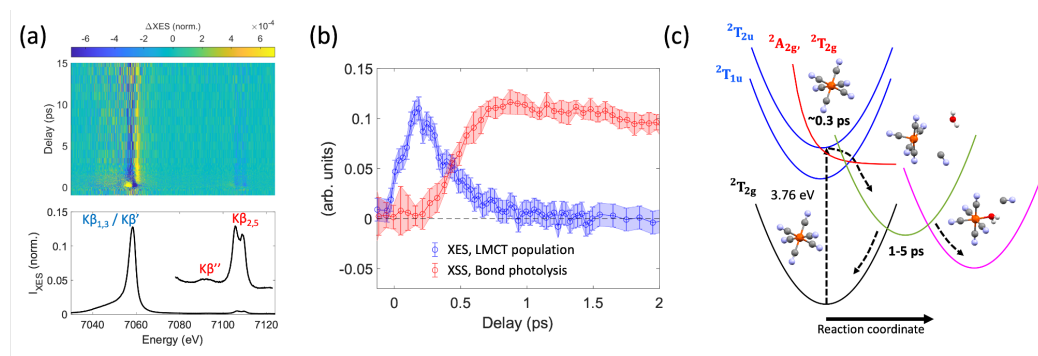
5.2. Simultaneous X-ray Solution Scattering and X-ray Emission Spectroscopy

Conducting simultaneous time-resolved XSS and XES measurements enables the observation of significant alterations in the intramolecular nuclear structure surrounding the metal center, while also shedding light on the charge and spin state of the relevant transition metal [46]. The integration of $K\alpha$, $K\beta$, and VtC region measurements, along with solution scattering, facilitates the concurrent monitoring of spin, geometric, and oxidation state changes while capturing structural dynamics [34,43,46]. This methodology was also employed to observe photo-induced electron transfer in a mixed valence Fe-Ru complex [36], light-induced spin crossover in $[\text{Fe}(\text{bpy})_3]^{2+}$ [68], and the photoinduced dynamics of the $[\text{Fe}(\text{bmip})_2]^{2+}$ photosensitizer [47].

For example, Reinhard *et al.* (2023) used simultaneous XSS-XES to elucidate the lifetime of a ligand-to-metal charge transfer (LMCT) state and the ground state recovery pathways of the aqueous ferricyanide anion $^2[\text{Fe}^{\text{III}}(\text{CN})_6]^{3-}$ following photoexcitation. The sample, 100 mM aqueous potassium hexacyanoferrate(III), flowed through a 50 μm diameter cylindrical liquid jet. An optical pump of 336 nm (3.6 μJ) and an X-ray probe centered at 8500 eV (5×10^{11} photons/pulse) were used at XCS. The optical pump had a 100 μm spot size diameter and 50 fs FWHM, while the X-ray probe had a 20 μm spot size diameter with 40 fs FWHM. An overall instrument response of 222 fs was used by the authors when fitting the data. The von Hamos spectrometer was equipped with four Ge(620) crystal analyzers that were set to cover an energy range of 7030 to 7125 eV with an energy resolution of 0.6 eV. The XES and XSS data presented is an average of 54 scans at (~ 7 min/scan) and an average of a subset of 8 scans, respectively, taking a total of approximately 7 hours to complete the acquisition of the full dataset.

The authors were able to measure difference spectra for the $K\beta$ main line and VtC region, respectively, as shown in **Figure 6a**. They reported two distinct populations of the difference spectra, the LMCT excited state and a longer-lived transient species. Comprehensive modeling of difference spectra in both $K\beta$ main line and VtC regions for various candidate transient species suggested that the species generated at 1-3 ps is a $^2[\text{Fe}^{\text{III}}(\text{CN})_5]^{2-}$ photo-aquation reaction intermediate. These results are supported by the XSS data, which exhibits a negative feature in the low- Q range $< 0.5 \text{ \AA}$ consistent with the loss of a cyanide ligand and the elongated Fe-cyanide bond distances of the $^2[\text{Fe}^{\text{III}}(\text{CN})_5]^{2-}$ intermediate. The onset of the scattering signal in the low- Q range is also delayed and only occurs as the LMCT excited state decays (**Figure 6b**), suggesting that ligand loss

659 follows the decay of the LMCT. By using both XSS and XES, the authors were able to
 660 determine the LMCT lifetime of ~ 0.3 ps and subsequent bond photolysis (**Figure 6c**)
 661 clarifying previous uncertainty in the excited state dynamics of the aqueous ferricyanide
 662 anion due to the inability to track and differentiate between the transient species
 663 generated.



664
665
666
667
668
669
670
Figure 6. (a) The time dependent difference spectra (top) corresponding to the changes in the $K\beta$ main line and VtC region emission (bottom) following photoexcitation. (b) A comparison between the LMCT population kinetics determined from XES (blue) and the scale low-Q range kinetics from XSS (red). A delayed onset of the low-Q range can clearly be seen. (c) Proposed relaxation scheme of $^2[Fe^{III}(CN)_6]^{3-}$ following photoexcitation at 336 nm. Figure adapted from Reinhard et al. (2023) with permission.

671 Beyond inner core XES, valence-to-core (VtC) XES provides further insights into the
 672 dynamics of solvated molecules. VtC is sensitive to both the geometric and electronic
 673 structure and recent developments at LCLS have enabled these challenging
 674 measurements for time-resolved studies of dilute systems [26,43].

675 Many applications at LCLS rely entirely on the XSS capability of observing structural
 676 changes. For example, those associated with the metal-metal bond cleavage of $Ru_3(CO)_{12}$,
 677 which was studied at XPP, revealing the sole chemical reaction is bond breakage [35]. XSS
 678 can be employed to probe the evolution of both ground and excited-state potential
 679 surfaces by mapping structural dynamics and monitoring distinct populations, facilitating
 680 the determination of the photoexcitation fraction and direct observation of ground-state
 681 structural dynamics [35,69]. Additionally, anisotropic contributions to solution scattering
 682 signals can be exploited to obtain information on structural dynamics pertaining to the
 683 directionality of the transition dipole-moment [70]. The anisotropy can further give
 684 insight into the symmetry of Raman excited molecular vibrations in solvents [71], and
 685 finally, the anisotropic signal can be leveraged for molecular insight while suppressing
 686 contributions from bulk solvent, such as heating [69]. Ultrafast XSS serves as a powerful
 687 tool for observing transient structural changes, although extensive modeling is typically
 688 performed alongside measurements to provide additional structural insight and aid in
 689 identifying the transient structures observed in the difference scattering signal [37,69].

690 6. Conclusions

691 X-ray free-electron lasers (XFELs) have transformed our ability to study and capture
 692 dynamic snapshots of materials, chemistry, and biology in action. To harness XFELs
 693 effectively, innovative sample delivery methods have emerged, specifically tailored to the
 694 unique characteristics of XFEL facilities. At the forefront of these advancements is the
 695 liquid jet endstation (LJE) setup, a standard configuration at the XCS instrument of the
 696 Linac Coherent Light Source (LCLS). This system has demonstrated remarkable results,
 697 enabling multimodal pump-probe studies that combine X-ray scattering and
 698 spectroscopic techniques such as X-ray solution scattering (XSS), X-ray emission
 699 spectroscopy (XES), and X-ray absorption spectroscopy (XAS). The LJE centers around a
 700 recirculating liquid jet that ensures fresh sample after each probe pulse at the 120 Hz LCLS

X-ray repetition rate. Additionally, it employs a diverse array of diagnostics and detectors designed for simultaneous X-ray spectroscopy and scattering experiments on solution-phase samples.

The use of the LJE at LCLS potentially allows researchers to probe the structure, spin, and charge of solution-phase systems with atomic resolution and elemental specificity. By coupling these methods with an optical laser system, solution-phase samples can be promptly photoexcited, and the ensuing ultrafast dynamics captured by the ultrashort XFEL pulses. The LJE has undergone various iterations and successfully supported experiments in material science, photochemistry and biochemistry in solution-phase systems. In summary, the LJE represents a remarkable synergy of novel capabilities, robust sample delivery, diagnostics and compact design serving the scientific community's needs at LCLS in answering fundamental questions about ultrafast dynamics of solution-phase systems. With the future LCLS upgrade, LCLS-II-HE will host a permanent endstation based on this system allowing for improvements in stability and reliability. This will facilitate even more standard and routine operation in addition to enabling further developments for the new frontier of experiments enabled by the higher repetition rate.

Author Contributions: Conceptualization: C.A., V.S.A., R.A-M. and T.v.D.; Writing – Original draft preparation: C.A., V.S.A.; Writing – Review and editing: C.A., V.S.A., G.C., R.R., S.L.R., J. T. B, P.S., L.G., A.T.G-E., R.A-M., T.v.D.; Laser: G.C., P.L.K.; XCS instrument resources and support: T.S., B.H., S.N., M.C.; Examples: M.R., R.R., D.S., L.G., A.T.G-E., J.L., J.T.B, A.H.F.; Visualization: T.v.D.; Supervision: R.A-M. and T.v.D; All authors have read and agreed to the published version of the manuscript.

Funding: This work was supported by NIH grant P41GM139687.

Data Availability Statement: The presented data can be made available upon request or through the cited references. Further example data or analysis code is available at LCLS upon contacting any of the instrument scientists.

Acknowledgments: We thank Jim Defever, Rob Paul and Serge Guillet for engineering support during design and manufacturing of the LJE. We also thank Robert E. Sublett and Wing Poi Chang for continued support, maintenance and deployment of liquid pumps at LCLS. We also wish to Thank James Glowonia for Laser developments and Patrick Opperman and Aalayah Spencer for controls, motors and camera integration of the LJE. Portions of this research were carried out at the Linac Coherent Light Source (LCLS) at the SLAC National Accelerator Laboratory. LCLS is an Office of Science User Facility operated for the US Department of Energy Office of Science by Stanford University.

Conflicts of Interest: The authors declare no conflicts of interest.

References

1. DePonte DP. Sample Delivery Methods: Liquids and Gases at FELs. In: Bergmann U, Yachandra V, Yano J, editors. X-Ray Free Electron Lasers: Applications in Materials, Chemistry and Biology. The Royal Society of Chemistry; 2017. pp. 323–336. doi:10.1039/9781782624097-00323
2. Koralek JD, Kim JB, Brůža P, Curry CB, Chen Z, Bechtel HA, et al. Generation and characterization of ultrathin free-flowing liquid sheets. *Nat Commun.* 2018;9: 1353. doi:10.1038/s41467-018-03696-w
3. Hoffman DJ, Van Driel TB, Kroll T, Crissman CJ, Ryland ES, Nelson KJ, et al. Microfluidic liquid sheets as large-area targets for high repetition XFELs. *Front Mol Biosci.* 2022;9: 1048932. doi:10.3389/fmolb.2022.1048932
4. van Driel TB, Nelson S, Armenta R, Blaj G, Boo S, Boutet S, et al. The ePix10k 2-megapixel hard X-ray detector at LCLS. *J Synchrotron Radiat.* 2020;27: 608–615. doi:10.1107/S1600577520004257
5. Hart P, Boutet S, Carini G, Dragone A, Duda B, Freytag D, et al. The Cornell-SLAC pixel array detector at LCLS. 2012 IEEE Nuclear Science Symposium and Medical Imaging Conference Record (NSS/MIC). IEEE; 2012. pp. 538–541. doi:10.1109/NSSMIC.2012.6551166
6. Blaj G, Dragone A, Kenney CJ, Abu-Nimeh F, Caragiulo P, Doering D, et al. Performance of ePix10K, a high dynamic range, gain auto-ranging pixel detector for FELs. Author(s); 2019. doi:10.1063/1.5084693

- 752 7. Feng Y, Feldkamp JM, Fritz DM, Cammarata M, Aymeric R, Caronna C, et al. A single-shot intensity-position monitor for hard
753 x-ray FEL sources. *X-ray Lasers and Coherent X-ray Sources: Development and Applications IX*. SPIE; 2011. pp. 163–168.
754 doi:10.1117/12.893740
- 755 8. Harmand M, Coffee R, Bionta MR, Chollet M, French D, Zhu D, et al. Achieving few-femtosecond time-sorting at hard X-ray
756 free-electron lasers. *Nat Photonics*. 2013;7: 215–218. doi:10.1038/nphoton.2013.11
- 757 9. Behrens C, Decker F-J, Ding Y, Dolgashev VA, Frisch J, Huang Z, et al. Few-femtosecond time-resolved measurements of X-ray
758 free-electron lasers. *Nat Commun*. 2014;5: 3762. doi:10.1038/ncomms4762
- 759 10. Bostedt C, Boutet S, Fritz DM, Huang Z, Lee HJ, Lemke HT, et al. Linac Coherent Light Source: The first five years. *Rev Mod*
760 *Phys*. 2016;88: 015007. doi:10.1103/RevModPhys.88.015007
- 761 11. Chollet M, Alonso-Mori R, Cammarata M, Damiani D, Defever J, Delor JT, et al. The X-ray Pump-Probe instrument at the Linac
762 Coherent Light Source. *J Synchrotron Radiat*. 2015;22: 503–507. doi:10.1107/S1600577515005135
- 763 12. Sierra RG, Batyuk A, Sun Z, Aquila A, Hunter MS, Lane TJ, et al. The Macromolecular Femtosecond Crystallography Instrument
764 at the Linac Coherent Light Source. *J Synchrotron Radiat*. 2019;26: 346–357. doi:10.1107/S1600577519001577
- 765 13. Alonso-Mori R, Caronna C, Chollet M, Curtis R, Damiani DS, Defever J, et al. The X-ray Correlation Spectroscopy instrument
766 at the Linac Coherent Light Source. *J Synchrotron Radiat*. 2015;22: 508–513. doi:10.1107/S1600577515004397
- 767 14. Narayanan S, Sandy A, Shu D, Sprung M, Preissner C, Sullivan J. Design and performance of an ultra-high-vacuum-compatible
768 artificial channel-cut monochromator. *J Synchrotron Radiat*. 2007;15: 12–18. doi:10.1107/S090904950705340X
- 769 15. Lemke HT, Bressler C, Chen LX, Fritz DM, Gaffney KJ, Galler A, et al. Femtosecond X-ray Absorption Spectroscopy at a Hard
770 X-ray Free Electron Laser: Application to Spin Crossover Dynamics. 2013 [cited 26 Mar 2024]. doi:10.1021/jp312559h
- 771 16. Britz A, Abraham B, Biasin E, van Driel TB, Gallo A, Garcia-Esparza AT, et al. Resolving structures of transition metal complex
772 reaction intermediates with femtosecond EXAFS. *Phys Chem Chem Phys*. 2020;22: 2660–2666. doi:10.1039/c9cp03483h
- 773 17. Kroll T, Weninger C, Fuller FD, Guetg MW, Benediktovitch A, Zhang Y, et al. Observation of Seeded Mn K β Stimulated X-Ray
774 Emission Using Two-Color X-Ray Free-Electron Laser Pulses. *Phys Rev Lett*. 2020;125: 037404.
775 doi:10.1103/PhysRevLett.125.037404
- 776 18. Decker F-J, Bane KL, Colocho W, Gilevich S, Marinelli A, Sheppard JC, et al. Tunable x-ray free electron laser multi-pulses with
777 nanosecond separation. *Sci Rep*. 2022;12: 3253. doi:10.1038/s41598-022-06754-y
- 778 19. Feng Y, Alonso-Mori R, Blank V, Boutet S, Chollet M, van Driel TB, et al. Recent development of thin diamond crystals for X-
779 ray FEL beam-sharing. *Advances in X-ray Free-Electron Lasers II: Instrumentation*. SPIE; 2013. pp. 26–33.
780 doi:10.1117/12.1518467
- 781 20. Bionta MR, Lemke HT, Cryan JP, Glowonia JM, Bostedt C, Cammarata M, et al. Spectral encoding of x-ray/optical relative delay.
782 *Opt Express*. 2011;19: 21855–21865. doi:10.1364/OE.19.021855
- 783 21. Glowonia JM, Gumerlock K, Lemke HT, Sato T, Zhu D, Chollet M. Pump-probe experimental methodology at the Linac Coherent
784 Light Source. *J Synchrotron Radiat*. 2019;26: 685–691. doi:10.1107/S160057751900225X
- 785 22. Bionta MR, Hartmann N, Weaver M, French D, Nicholson DJ, Cryan JP, et al. Spectral encoding method for measuring the
786 relative arrival time between x-ray/optical pulses. *Rev Sci Instrum*. 2014;85: 083116. doi:10.1063/1.4893657
- 787 23. Stan CA, Milathianaki D, Laksmono H, Sierra RG, McQueen TA, Messerschmidt M, et al. Liquid explosions induced by X-ray
788 laser pulses. *Nat Phys*. 2016;12: 966–971. doi:10.1038/nphys3779
- 789 24. Vagovič P, Sato T, Mikeš L, Mills G, Graceffa R, Mattsson F, et al. Megahertz x-ray microscopy at x-ray free-electron laser and
790 synchrotron sources. *Optica*. 2019;6: 1106. doi:10.1364/optica.6.001106
- 791 25. Lemke HT, Kjær KS, Hartsock R, van Driel TB, Chollet M, Glowonia JM, et al. Coherent structural trapping through wave packet
792 dispersion during photoinduced spin state switching. *Nat Commun*. 2017;8: 15342. doi:10.1038/ncomms15342
- 793 26. Reinhard M, Gallo A, Guo M, Garcia-Esparza AT, Biasin E, Qureshi M, et al. Ferricyanide photo-aquation pathway revealed by
794 combined femtosecond K β main line and valence-to-core x-ray emission spectroscopy. *Nat Commun*. 2023;14: 2443.
795 doi:10.1038/s41467-023-37922-x
- 796 27. Choi EH, Lee Y, Heo J, Ihee H. Reaction dynamics studied via femtosecond X-ray liquidography at X-ray free-electron lasers.
797 *Chem Sci*. 2022;13: 8457–8490. doi:10.1039/d2sc00502f
- 798 28. Khakhulin D, Otte F, Biednov M, Bömer C, Choi T-K, Diez M, et al. Ultrafast X-ray Photochemistry at European XFEL:
799 Capabilities of the Femtosecond X-ray Experiments (FXE) Instrument. *NATO Adv Sci Inst Ser E Appl Sci*. 2020;10: 995.
800 doi:10.3390/app10030995
- 801 29. Carini GA, Alonso-Mori R, Blaj G, Caragiulo P, Chollet M, Damiani D, et al. Studies of the ePix100 low-noise x-ray camera at
802 SLAC. 2014 IEEE Nuclear Science Symposium and Medical Imaging Conference (NSS/MIC). IEEE; 2014. pp. 1–3.
803 doi:10.1109/NSSMIC.2014.7431079
- 804 30. Barends TRM, Gorel A, Bhattacharyya S, Schirò G, Bacellar C, Cirelli C, et al. Influence of pump laser fluence on ultrafast
805 myoglobin structural dynamics. *Nature*. 2024;626: 905–911. doi:10.1038/s41586-024-07032-9
- 806 31. Stickrath AB, Mara MW, Lockard JV, Harpham MR, Huang J, Zhang X, et al. Detailed transient heme structures of Mb-CO in
807 solution after CO dissociation: an X-ray transient absorption spectroscopic study. *J Phys Chem B*. 2013;117: 4705–4712.
808 doi:10.1021/jp3086705
- 809 32. Arcovito A, Lamb DC, Nienhaus GU, Hazemann JL, Benfatto M, Della Longa S. Light-induced relaxation of photolyzed
810 carbonmonoxy myoglobin: a temperature-dependent x-ray absorption near-edge structure (XANES) study. *Biophys J*. 2005;88:
811 2954–2964. doi:10.1529/biophysj.104.054973

- 812 33. Della Longa S, Arcovito A, Girasole M, Hazemann JL, Benfatto M. Quantitative analysis of x-ray absorption near edge structure
813 data by a full multiple scattering procedure: the Fe-CO geometry in photolyzed carbonmonoxy-myoglobin single crystal. *Phys*
814 *Rev Lett.* 2001;87: 155501. doi:10.1103/PhysRevLett.87.155501
- 815 34. Gaffney KJ. Capturing photochemical and photophysical transformations in iron complexes with ultrafast X-ray spectroscopy
816 and scattering. *Chem Sci.* 2021;12: 8010–8025. doi:10.1039/d1sc01864g
- 817 35. Kong QY, Laursen MG, Haldrup K, Kjær KS, Khakhulin D, Biasin E, et al. Initial metal-metal bond breakage detected by fs X-
818 ray scattering in the photolysis of Ru₃(CO)₁₂ in cyclohexane at 400 nm. *Photochem Photobiol Sci.* 2019;18: 319–327.
819 doi:10.1039/c8pp00420j
- 820 36. Biasin E, Fox ZW, Andersen A, Ledbetter K, Kjær KS, Alonso-Mori R, et al. Direct observation of coherent femtosecond solvent
821 reorganization coupled to intramolecular electron transfer. *Nat Chem.* 2021;13: 343–349. doi:10.1038/s41557-020-00629-3
- 822 37. van Driel TB, Kjær KS, Hartsock RW, Dohn AO, Harlang T, Chollet M, et al. Atomistic characterization of the active-site
823 solvation dynamics of a model photocatalyst. *Nat Commun.* 2016;7: 1–7. doi:10.1038/ncomms13678
- 824 38. Kjær KS, van Driel TB, Kehres J, Haldrup K, Khakhulin D, Bechgaard K, et al. Introducing a standard method for experimental
825 determination of the solvent response in laser pump, X-ray probe time-resolved wide-angle X-ray scattering experiments on
826 systems in solution. *Phys Chem Chem Phys.* 2013;15: 15003–15016. doi:10.1039/C3CP50751C
- 827 39. Prins R, Koningsberger DC. *Catalysis. X-ray absorption : principles, applications, techniques of EXAFS, SEXAFS and XANES.*
828 Wiley; 1988. pp. 321–372. Available: <https://tue.elsevierpure.com/en/publications/catalysis>
- 829 40. Yano J, Yachandra VK. X-ray absorption spectroscopy. *Photosynth Res.* 2009;102: 241–254. doi:10.1007/s11120-009-9473-8
- 830 41. Alonso-Mori R, Kern J, Sokaras D, Weng T-C, Nordlund D, Tran R, et al. A multi-crystal wavelength dispersive x-ray
831 spectrometer. *Rev Sci Instrum.* 2012;83: 073114. doi:10.1063/1.4737630
- 832 42. spectra.tools. [cited 1 Apr 2024]. Available: https://www.spectra.tools/bin/controller.pl?body=Bragg_Angle_Calculator
- 833 43. Ledbetter K, Reinhard ME, Kunnus K, Gallo A, Britz A, Biasin E, et al. Excited state charge distribution and bond expansion of
834 ferrous complexes observed with femtosecond valence-to-core x-ray emission spectroscopy. *J Chem Phys.* 2020;152: 074203.
835 doi:10.1063/1.5139441
- 836 44. March AM, Doumy G, Andersen A, Al Haddad A, Kumagai Y, Tu M-F, et al. Elucidation of the photoaquation reaction
837 mechanism in ferrous hexacyanide using synchrotron x-rays with sub-pulse-duration sensitivity. *J Chem Phys.* 2019;151:
838 144306. doi:10.1063/1.5117318
- 839 45. Reinhard M, Penfold TJ, Lima FA, Rittmann J, Rittmann-Frank MH, Abela R, et al. Photooxidation and photoaquation of iron
840 hexacyanide in aqueous solution: A picosecond X-ray absorption study. *Struct Dyn.* 2014;1: 024901. doi:10.1063/1.4871751
- 841 46. Kjær KS, Van Driel TB, Harlang TCB, Kunnus K, Biasin E, Ledbetter K, et al. Finding intersections between electronic excited
842 state potential energy surfaces with simultaneous ultrafast X-ray scattering and spectroscopy. *Chem Sci.* 2019;10: 5749–5760.
843 doi:10.1039/c8sc04023k
- 844 47. Kunnus K, Vacher M, Harlang TCB, Kjær KS, Haldrup K, Biasin E, et al. Vibrational wavepacket dynamics in Fe carbene
845 photosensitizer determined with femtosecond X-ray emission and scattering. *Nat Commun.* 2020;11: 634. doi:10.1038/s41467-
846 020-14468-w
- 847 48. Mara MW, Hadt RG, Reinhard ME, Kroll T, Lim H, Hartsock RW, et al. Metalloprotein entatic control of ligand-metal bonds
848 quantified by ultrafast x-ray spectroscopy. *Science.* 2017;356: 1276–1280. doi:10.1126/science.aam6203
- 849 49. Penfold TJ, Reinhard M, Rittmann-Frank MH, Tavernelli I, Rothlisberger U, Milne CJ, et al. X-ray spectroscopic study of solvent
850 effects on the ferrous and ferric hexacyanide anions. *J Phys Chem A.* 2014;118: 9411–9418. doi:10.1021/jp5055588
- 851 50. Ross M, Andersen A, Fox ZW, Zhang Y, Hong K, Lee J-H, et al. Comprehensive Experimental and Computational Spectroscopic
852 Study of Hexacyanoferrate Complexes in Water: From Infrared to X-ray Wavelengths. *J Phys Chem B.* 2018;122: 5075–5086.
853 doi:10.1021/acs.jpcc.7b12532
- 854 51. Hayakawa K, Hatada K, D'Angelo P, Della Longa S, Natoli CR, Benfatto M. Full quantitative multiple-scattering analysis of X-
855 ray absorption spectra: application to potassium hexacyanoferrate(II) and -(III) complexes. *J Am Chem Soc.* 2004;126: 15618–
856 15623. doi:10.1021/ja045561v
- 857 52. Westre TE, Kennepohl P, DeWitt JG, Hedman B, Hodgson KO, Solomon EI. Understanding Fe K-edge XAS pre-edge features:
858 A multiplet analysis of the 1s-> 3d final states. *ABSTRACTS OF PAPERS OF THE AMERICAN CHEMICAL SOCIETY. AMER*
859 *CHEMICAL SOC 1155 16TH ST, NW, WASHINGTON, DC 20036; 1997.* p. 485–INOR.
- 860 53. Sension RJ, McClain TP, Lamb RM, Alonso-Mori R, Lima FA, Ardana-Lamas F, et al. Watching Excited State Dynamics with
861 Optical and X-ray Probes: The Excited State Dynamics of Aquocobalamin and Hydroxocobalamin. *J Am Chem Soc.* 2023;145:
862 14070–14086. doi:10.1021/jacs.3c04099
- 863 54. Miller NA, Michocki LB, Konar A, Alonso-Mori R, Deb A, Glowonia JM, et al. Ultrafast XANES Monitors Femtosecond Sequential
864 Structural Evolution in Photoexcited Coenzyme B12. *J Phys Chem B.* 2020;124: 199–209. doi:10.1021/acs.jpcc.9b09286
- 865 55. Michocki LB, Miller NA, Alonso-Mori R, Britz A, Deb A, Glowonia JM, et al. Probing the Excited State of Methylcobalamin Using
866 Polarized Time-Resolved X-ray Absorption Spectroscopy. *J Phys Chem B.* 2019;123: 6042–6048. doi:10.1021/acs.jpcc.9b05854
- 867 56. Cammarata M, Zerdane S, Balducci L, Azzolina G, Mazerat S, Exertier C, et al. Charge transfer driven by ultrafast spin transition
868 in a CoFe Prussian blue analogue. *Nat Chem.* 2021;13: 10–14. doi:10.1038/s41557-020-00597-8
- 869 57. Vester P, Kubicek K, Alonso-Mori R, Assefa T, Biasin E, Christensen M, et al. Tracking structural solvent reorganization and
870 recombination dynamics following e- photoabstraction from aqueous I- with femtosecond x-ray spectroscopy and scattering. *J*
871 *Chem Phys.* 2022;157: 224201. doi:10.1063/5.0107224

- 872 58. Holm RH, Kennepohl P, Solomon EI. Structural and Functional Aspects of Metal Sites in Biology. *Chem Rev.* 1996;96: 2239–
873 2314. doi:10.1021/cr9500390
- 874 59. Williams JAG. Photochemistry and Photophysics of Coordination Compounds: Platinum. In: Balzani V, Campagna S, editors.
875 Photochemistry and Photophysics of Coordination Compounds II. Berlin, Heidelberg: Springer Berlin Heidelberg; 2007. pp.
876 205–268. doi:10.1007/128_2007_134
- 877 60. Chergui M. Ultrafast photophysics of transition metal complexes. *Acc Chem Res.* 2015;48: 801–808. doi:10.1021/ar500358q
- 878 61. Rehr JJ, Mustre de Leon J, Zabinsky SI, Albers RC. Theoretical x-ray absorption fine structure standards. *J Am Chem Soc.*
879 1991;113: 5135–5140. doi:10.1021/ja00014a001
- 880 62. Duchesne PN, Chen G, Zheng N, Zhang P. Local Structure, Electronic Behavior, and Electrocatalytic Reactivity of CO-Reduced
881 Platinum–Iron Oxide Nanoparticles. *J Phys Chem C.* 2013;117: 26324–26333. doi:10.1021/jp4093496
- 882 63. Hersbach TJP, Garcia AC, Kroll T, Sokaras D, Koper MTM, Garcia-Esparza AT. Base-Accelerated Degradation of Nanosized
883 Platinum Electrocatalysts. *ACS Catal.* 2021;11: 9904–9915. doi:10.1021/acscatal.1c02468
- 884 64. Glebov EM, Pozdnyakov IP, Plyusnin VF, Khmelinskii I. Primary reactions in the photochemistry of hexahalide complexes of
885 platinum group metals: A minireview. *J Photochem Photobiol C: Photochem Rev.* 2015;24: 1–15.
886 doi:10.1016/j.jphotochemrev.2015.05.003
- 887 65. Levantino M, Lemke HT, Schirò G, Glownia M, Cupane A, Cammarata M. Observing heme doming in myoglobin with
888 femtosecond X-ray absorption spectroscopy. *Struct Dyn.* 2015;2: 041713. doi:10.1063/1.4921907
- 889 66. Mills DM, Lewis A, Harootunian A, Huang J, Smith B. Time-Resolved X-ray Absorption Spectroscopy of Carbon Monoxide-
890 Myoglobin Recombination After Laser Photolysis. *Science.* 1984;223: 811–813. doi:10.1126/science.223.4638.811
- 891 67. Wang H, Peng G, Cramer SP. X-ray absorption spectroscopy of biological photolysis products: kilohertz photolysis and soft X-
892 ray applications. *J Electron Spectrosc Relat Phenom.* 2005;143: 1–7. doi:10.1016/j.elspec.2004.10.011
- 893 68. Kjær KS, Kunnus K, Harlang TCB, Van Driel TB, Ledbetter K, Hartsock RW, et al. Solvent control of charge transfer excited
894 state relaxation pathways in [Fe(2,2'-bipyridine)(CN)₄]₂. *Phys Chem Chem Phys.* 2018;20: 4238–4249. doi:10.1039/c7cp07838b
- 895 69. Haldrup K, Levi G, Biasin E, Vester P, Laursen MG, Beyer F, et al. Ultrafast X-Ray Scattering Measurements of Coherent
896 Structural Dynamics on the Ground-State Potential Energy Surface of a Diplatinum Molecule. *Phys Rev Lett.* 2019;122: 063001.
897 doi:10.1103/PhysRevLett.122.063001
- 898 70. Biasin E, van Driel TB, Levi G, Laursen MG, Dohn AO, Moltke A, et al. Anisotropy enhanced X-ray scattering from solvated
899 transition metal complexes. *J Synchrotron Radiat.* 2018;25: 306–315. doi:10.1107/S1600577517016964
- 900 71. Montoya-Castillo A, Chen MS, Raj SL, Jung KA, Kjaer KS, Morawietz T, et al. Optically Induced Anisotropy in Time-Resolved
901 Scattering: Imaging Molecular-Scale Structure and Dynamics in Disordered Media with Experiment and Theory. *Phys Rev Lett.*
902 2022;129: 056001. doi:10.1103/PhysRevLett.129.056001

903 **Disclaimer/Publisher's Note:** The statements, opinions and data contained in all publications are solely those of the individual
904 author(s) and contributor(s) and not of MDPI and/or the editor(s). MDPI and/or the editor(s) disclaim responsibility for any injury
905 to people or property resulting from any ideas, methods, instructions or products referred to in the content.